Theor Chem Acc (2011) 129:847–857
DOI 10.1007/s00214-011-0943-7

REGULAR ARTICLE

DFT study of structure–properties correlations in [MnTPP][TCNE] quasi-one-dimensional molecular magnets

Corneliu I. Oprea · Fanica Cimpoesu · Petre Panait · Bogdan Frecuş · Marilena Ferbinteanu · Mihai A. Gîrţu

Received: 23 December 2010 / Accepted: 12 April 2011 / Published online: 18 May 2011

Abstract We report the first band structure calculations of the quasi-one-dimensional [MnTPP][TCNE] compounds (TPP = *meso*-tetraphenylporphyrinato, TCNE = tetracyanoethylene), based on Density Functional Theory (DFT) methods, in order to interpret the magnetic ordering in these prototypic systems. We compare and contrast the results of broken-symmetry DFT calculations for extended systems, with periodic boundary conditions, and for finite systems, magnetic dimers modeling the actual molecular magnets. By varying systematically the main angles, we are able to determine the geometry dependence of the exchange interaction. Structure–properties correlations in these charge-transfer salts reveal the determinant role of the Mn-$(N\equiv C)_{TCNE}$ bond angle on the strength of the ferrimagnetic coupling between the $S_1 = 2$ spin located on the Mn^{III}-porphyrin donor and the $S_2 = 1/2$ spin positioned on the cyanocarbon acceptor. When the Mn-$(N\equiv C)_{TCNE}$ angle is decreased, the intrachain magnetic coupling strengthens, correlated with the increase in the $d_{z^2} - \pi*$ orbital overlap. The exchange coupling constants resulting from DFT calculations of extended systems, with periodic boundary conditions, were found to be consistent with those obtained for the dimers, but systematically smaller. The exchange constants vary strongly with the functional used, hybrid functionals such as B3LYP leading to results that better correlate with the experimental mean-field critical temperatures. The coupling constant varies significantly with the type of broken-symmetry approach, depending on the overlap between magnetic orbitals, but weakly on the basis set once polarization effects are included. The electronic structure calculations for the extended systems provide a density of states consistent with the energy spectrum of the corresponding dimer, allowing for an intuitive explanation of the intrachain ferrimagnetic ordering.

Keywords Molecular magnets · Single chain magnets · Manganese-porphyrin compounds · Exchange coupling · Density functional theory · Broken symmetry

Electronic supplementary material The online version of this article (doi:10.1007/s00214-011-0943-7) contains supplementary material, which is available to authorized users.

C. I. Oprea · P. Panait · B. Frecuş · M. A. Gîrţu (✉)
Department of Physics, Ovidius University of Constanţa, 900527 Constanţa, Romania
e-mail: girtu@univ-ovidius.ro

F. Cimpoesu (✉)
Department of Theoretical Chemistry, Institute of Physical Chemistry, 060021 Bucharest, Romania
e-mail: cfanica@yahoo.com

B. Frecuş
Department of Theoretical Chemistry, Royal Institute of Technology, 106 91 Stockholm, Sweden

M. Ferbinteanu
Department of Inorganic Chemistry, University of Bucharest, 020462 Bucharest, Romania

1 Introduction

Molecular magnets are materials in which electrons in molecular orbitals play a crucial role in the magnetic ordering [1–3]. In some of these systems, the organic constituents play an active role, with unpaired spins delocalized over the organic species. Examples of such molecular magnets are the $[Mn^{III}(porphyrin)]^+[cyanocarbon]^-$ charge-transfer salts with a net spin on the ligand [4–14].

The family of metalloporphyrin-based magnets has stirred special interest as it provides an unusual opportunity for the study of magnetic ordering because of its wide range of controlling factors [15]. For example, the cyanocarbon bridge connecting the adjacent porphyrins can be varied to influence the intrachain interactions [16, 17], different organic constituents can be added at the periphery of the porphyrin to affect the interchain interactions and, thereby, build up or reduce three-dimensional magnetic order [18, 19], various solvents that may induce glassy behavior [20, 21] can be incorporated into the structure, leading to properties attributed later to single chain magnets [3, 22]. Extensive experimental studies performed to understand the role of the different building blocks forming these materials, revealed interesting magnetic properties (one-dimensional ferrimagnetic behavior at high temperatures [16, 17], three-dimensional canted antiferromagnetic or weak ferromagnetic behavior at low temperatures [19]) and phenomena (lattice- and/or spin-dimensionality crossovers [18]).

The first member of the family was [MnTPP][TCNE]·*x*S [4], where (TPP = *meso*-tetraphenylporphyrinato, TCNE = tetracyanoethylene, and S = toluene). Since then a large variety of related compounds has been synthesized and characterized [5–14]. The manganese-porphyrin compounds are quasi-one-dimensional electron-transfer salts consisting of chains of alternating metalloporphyrin electron donors and cyanocarbon electron acceptors. The adjacent spins along these chain alternates $S_1 = 2$ on the donor and $S_2 = 1/2$ on the acceptor.

The mechanism for magnetic ordering proposed [16, 17] for the manganese-porphyrin compounds [MnTPP][TCNE]·*x*S, (S = toluene, *ortho*-xylene, *ortho*-dichlorobenzene, etc.) is based on strong intrachain exchange, weak interchain dipole–dipole interactions, and modest single-ion anisotropy, all leading to canted magnetic ordering at low temperatures. The mechanism was based on the results of fits of the dc susceptibility data to a model of alternating classical and quantum spins [23], which provided exchange constants of about −70 to −140 K, for certain [MnTPP][TCNE]·*x*S systems [14, 16, 17]. Generally, the fit was good in the range 50–350 K but at low temperatures deviations occurred, attributed to interchain interactions. The antiferromagnetic coupling along the chain of unequal alternating spins leads to a 1D ferrimagnetic spin configuration. Then, in the absence of superexchange pathways between the chains, the classical dipole–dipole interaction (coupling of about 10^{-3}–10^{-2} K) together with the onsite single-ion anisotropy (estimated to about 1–3 K) were proposed to produce canted magnets with critical temperatures around 10–15 K [16, 17].

Despite extensive experimental studies, rigorous theoretical confirmations of the magnetic ordering mechanism have been lacking. A first theoretical approach by Kollmar et al. [24] succeeded in correlating the mean-field critical temperatures with the overlap between the d_{Z^2} orbital of $[\text{Mn-porphyrin}]^+$ and the π^* molecular orbital of $[\text{TCNE}]^{\cdot -}$. Later on, CASSCF, CASPT2, and DFT/B3LYP calculations by Novoa et al. [25] qualitatively reproduced the antiferromagnetic intrachain coupling and ferrimagnetic spin configuration along the chains. It was found that the DFT techniques tend to overestimate the experimental exchange coupling constant, whereas the ab initio approaches underestimate them. Based on the results obtained, it was impossible to assign the mechanism of magnetic ordering in this family of compounds [25].

Broken-symmetry (BS) DFT studies of the manganese–porphyrin–cyanocarbon dimer provided antiferromagnetic exchange constants of different strengths, depending on the functional used [26]. In that case, all DFT results underestimated the experimental value, obtained based on the Seiden fit, best results being obtained with the B3LYP functional. More recently, other BS/DFT calculations studied the role of the Mn-TCNE bonding geometry on the intrachain exchange and demonstrated that the phenyl substituent has a small influence on the intrachain coupling and confirmed that the values of exchange constant depend strongly on the DFT functional used [27]. However, these studies did not address the theoretical basis of the spin coupling mechanism sought by Novoa et al. [25].

We report here first broken-symmetry DFT numerical calculations on models of Mn–porphyrin–cyanocarbon systems, providing the intrachain exchange coupling constant and its dependence on geometrical parameters for extended systems, using periodic boundary conditions. The band calculations for the extended system are compared with the computations for dimers. We also compare the results of the main three broken-symmetry approaches as well as the role of the DFT functional and of the basis sets on the value of the exchange constant. Based on magneto-structural correlations, we build on the studies by Kollmar et al. [24] and Novoa et al. [25], to understand the mechanism of ferrimagnetic ordering in these systems and we discuss the use of BS/DFT for modeling molecular magnets.

2 The broken-symmetry approach

The magnetic interaction between two localized spins is generically expressed in terms the well-known Heisenberg–Dirac–van Vleck (HDvV) Hamiltonian, describing isotropic symmetric exchange [1, 2]:

$$H_{\mathrm{HDvV}} = -2JS_1 \cdot S_2, \tag{1}$$

The HDvV Hamiltonian commutes with $\mathbf{S}^2$ and S_z, where $\mathbf{S} = \mathbf{S}_1 + \mathbf{S}_2$; therefore, the three operators have a common set of eigenvalues, labeled by S and S_z. In order to determine the exchange coupling constant by means of Eq. 1, the energies of all the S spin multiplets between $|S_1 - S_2|$ and $S_{\mathrm{HS}} = S_1 + S_2$ should be computed. For multiconfiguration methods, all the spin states of the system are available, with a heavy price in terms of computational efforts. In contrast, DFT methods are much less demanding but the limitation is that, being intrinsically a single determinant method, it is impossible to provide the full spectrum of S states. Except for the high-spin one, S_{HS}, which can be well described by a single determinant, all the other states are multiconfigurational. Particularly, the state corresponding to the lowest spin is a linear combination of Slater determinants that are eigenstates of S_z with eigenvalue $|S_1 - S_2|$.

The treatment of the open-shell states of the magnetic system within the DFT methods [28–30] is based on spin-polarized or unrestricted DFT calculations in combination with the broken-symmetry (BS) approach [31–36]. This approach has proven to be a powerful tool in the prediction and interpretation of magnetic properties of a large variety of magnetic systems, as well as for revealing and tracing magneto-structural correlations [37]. The broken-symmetry treatment results in a solution that is an eigenstate of S_z (with eigenvalue S_{min}) but not of $\mathbf{S}^2$, which can be written as a weighted average of the energies of the pure spin multiplets. The literature shows various ways of interpreting the results of BS/DFT calculation, to estimate the J coupling parameter [31–36]. In the case of a spin dimer, they all have in common the energy difference between the high-spin and the BS states. The first BS/DFT calculation was performed by Noodleman et al., using the expression [31, 32, 38]:

$$2J_N = -\frac{E_{\mathrm{HS}} - E_{\mathrm{BS}}}{2S_1S_2}, \tag{2}$$

obtained in the approximation of orthogonal magnetic orbitals on the two centers. This approximation is applicable only in the weak overlap limit, and the strength of the exchange coupling constants obtained has been systematically larger than the experimental values. An alternative formula proposed by Ruiz et al. [39, 40]

$$2J_R = -\frac{E_{\mathrm{HS}} - E_{\mathrm{BS}}}{2S_1S_2 + S_2}, \tag{3}$$

($S_1 \geq S_2$) was derived in the strong overlap limit. The approximate projection method was introduced by Yamaguchi et al. to account for the overlap between the magnetic orbitals ant to consider the spin contamination, especially of the BS state [36, 41, 42]

$$2J_Y = -2\frac{E_{\mathrm{HS}} - E_{\mathrm{BS}}}{\langle S^2\rangle_{\mathrm{HS}} - \langle S^2\rangle_{\mathrm{BS}}}, \tag{4}$$

in the approximate spin projected scheme. This procedure, implying unrestricted DFT calculations for the system in both the BS state and the HS state, based on the total energies and the expectation values of the square of the spin, has provided exchange values intermediate between those obtained with Eqs. 2 and 3.

So far, we have focused our attention to the HDvV Hamiltonian, describing isotropic symmetric exchange. The anisotropic Ising Hamiltonian [1, 2]

$$H_I = -2\,JS_1^zS_2^z \tag{5}$$

does not commute with the HDvV Hamiltonian. However, it has been shown [43], that, in the BS/DFT approach, the Ising Hamiltonian provides a description of the HS and BS spin states identical with the HDvV Hamiltonian in the weak overlap limit, such that for the binuclear spin system the resulting exchange constant is given by an expression identical to Eq. 2.

The BS/DFT method has been applied successfully to systems with two spin centers and generalized by Yamaguchi et al. to multispin systems [44], again based on the handling of the $\langle S^2\rangle$ expectation values for the various spin-flip configurations. It is worth mentioning that in certain particular topologies, such as the symmetric trimer (with J coupling only between adjacent centers and no next-nearest-neighbor interaction), Eq. 4 remains literally valid beyond the case of the dimer [45].

The BS/DFT method has been extensively applied to dimers and even to multispin clusters, but less commonly to extended systems, using periodic boundary conditions. Yamaguchi et al. recently approached the problem of an $(\mathrm{A} - \mathrm{B})_n$ system, comparing the results obtained for finite systems, based on the approximate projection method with those calculated for extended ones within the Ising model [46].

It is important to note that to be applied to extended systems with PBCs the exchange constant provided by the Ising approach should be amended by a factor of 1/2, for topological reasons, as each center is biconnected in the infinite chain but simply connected in the dimer. In the Ising frame, we have:

$$H_I = -2\,J\sum_{i=1}^{n}\left(S_{1,i}^zS_{2,i}^z + S_{2,i}^zS_{1,i+1}^z\right), \tag{6}$$

such that the energies of the extended system with n unit cells are $\tilde{E}_{\mathrm{HS}} = -4nJ|S_1||S_2|$ and $\tilde{E}_{\mathrm{LS}} = +4nJ|S_1||S_2|$, resulting in an exchange coupling of $2J = -(\tilde{E}_{\mathrm{HS}} - \tilde{E}_{\mathrm{BS}})/(4n|S_1||S_2|)$. By expressing the energy per unit cell, which translates into dividing the energies by n, i.e. $\tilde{E}/n \rightarrow E$, the magnetic constant determined with PBCs is:

$$2J_{\mathrm{PBC}} = -\frac{E_{\mathrm{HS}} - E_{\mathrm{BS}}}{4|S_1||S_2|}. \quad (7)$$

3 Computation details

The chains of [MnTPP][TCNE] have an alternating structure of $[MnTPP]^+$ cations and $[TCNE]^-$ anions. According to the rules of addition of angular momenta, the coupling between the $S_1 = 2$ and $S_2 = 1/2$ radicals leads to two possible states: an $S_{\mathrm{HS}} = 5/2$ high-spin state and an $S_{\mathrm{LS}} = 3/2$ low-spin state. In this case, a simple calculation based on Eq. 1 leads to the analytic expression.

The $[MnTPP]^+[TCNE]^{\cdot -}$ systems were modeled with an Li^+ ion added to the terminal CN group of the $[TCNE]^-$ radical (to mimic the polarization effects of the next metal ion) and an HCN group *trans* coordinated to Mn^{III}, used as a substitute for the TCNE on the other side of the porphyrin (to insure hexacoordination of the metal ion). Further idealization was done replacing the phenyl groups with H atoms and symmetrizing the slight deviation from the tetragonal symmetry, optimizing the model of simple porphyrin within D_{4h} point group. The $[TCNE]^{\cdot -}$ anion was separately optimized within D_{2h} using DFT/BP86/6-31G(d) method. We showed in earlier work that the phenyl groups have minor influence on the strength of the intrachain magnetic interaction [27], but play a major role in the interchain interactions [16, 17]. The resulting dimer proposed as a model for $[MnTPP]^+[TCNE]^-$ systems is $\{(HCN)[Mn^{III}P]^+[TCNE]^-Li^+\}$, shown in Fig. 1.

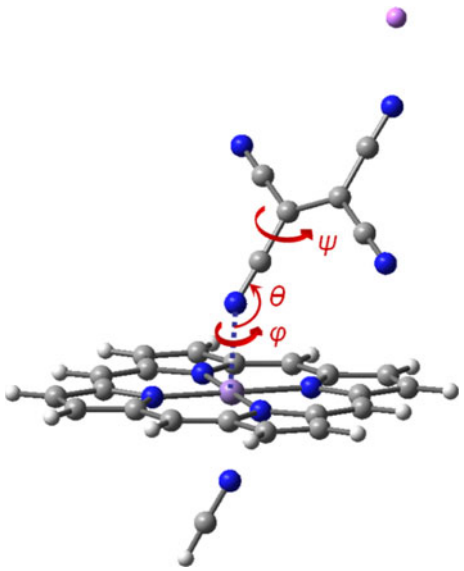

Fig. 1 Structure of the $\{(HCN)[Mn^{III}P]^+[TCNE]^-Li^+\}$ system used to model exchange interactions in $[MnTPP]^+[TCNE]^-$. The internal coordinates essential for describing the geometry and making the structure–properties correlations are indicated in *red*

The key parameters used in our attempt to correlate the structure and the strength of the intrachain magnetic interaction have been (see Fig. 1) the $Mn–N_{TCNE}$ distance, r, the $Mn–(N\equiv C)_{TCNE}$ angle, θ, the Mn–(N≡C–N)TCNE dihedral angle, ψ (which defines the rotation of the TCNE plane around the line along the N≡C–group coordinated to Mn) and the Npor–Mn–(N≡C)TCNE dihedral angle, φ (which defines the rotation of the TCNE plane around the line connecting the Mn ion and the N_{TCNE} atom coordinated to it). Although this is neither a unique nor a complete set of coordinates, it captures the essence of the various interaction geometries and allows the comparison with other theoretical studies as well as experimental results.

Calculations were also performed for extended systems, using periodic boundary conditions (PBC). The elementary cell, consisting of $[Mn^{III}P]^+[TCNE]^-$, for straightforward comparison with the dimer calculations, was varied by changing the key parameters mentioned elsewhere and adjusting correspondingly the translation vector.

Unrestricted DFT calculations were carried out for both the dimers and the extended systems with PBC with the Gaussian03 [47] package. The exchange maps and the low-spin energy surfaces for various spatial configurations of both the dimer and the extended system were obtained using the generalized gradient approximation functional BP86 [48, 49] with double zeta polarized 6-31G* basis sets [50] for Mn, TCNE and $N_{por,}$ and 6-31G functions for all other atoms. The optimization of the extended system was performed by DFT/BP86/6-31G* basis sets. This optimized geometry was further used for a comparison of the role of the functional and of the basis set on the exchange constant. Two gradient corrected functionals, BP86 [49, 51] and BLYP [51, 52], and a hybrid functional B3LYP [52, 53] were used with various basis sets: 6-31G*, 6-31+G* (augmented with diffuse functions), as well as triple zeta polarized 6-311G* functions [50] for Mn, TCNE and N_{por}, and 6-31G functions for all other atoms. The density of states calculations was performed at DFT/BP86/6-31+G* level on the optimized geometry.

We showed earlier that once polarization effects are included, the differences between the basis sets do not lead to significant variations of the exchange constants [27]. The functional, however, exerts a sensible role, BP86 giving higher absolute values of J, compared with B3LYP [27]. The choice of the functional combined arguments of performance as well as economy of the calculations. Keeping in mind the much higher demands of the band computations, we used the BP86 functional to draw the exchange maps, but relied on the more accurate B3LYP hybrid functional with the 6-31G* basis set when we compared the results of the calculations for the dimer with the experimental results.

4 Results and discussion

4.1 Calculated exchange maps and magneto-structural correlations

The BS/DFT calculations were performed for the HS and LS states imposing a sextet or a quartet multiplicity, respectively, for a variety of angles θ, φ, and ψ, and both for the dimers and for the extended system, under PBC. The computations were performed at intervals of 15° for all three angles, fixing the distance between the Mn ion and the coordinating N_{TCNE} at $r = 2.300$ Å (chosen as an average of the experimental values [12–14]). The ranges for the main angles stopped at $\theta = 120°$ and at $\psi = 135°$ due to the sterical hindrance encountered at this conformation between the TCNE and the porphyrin when the plane of the cyanocarbon bridge is tilted excessively. In these linear chain compounds, the $[Mn(porphyrin)]^+$ cations are bridged by $[TCNE]^{\cdot-}$ anions in a *trans*-μ-N-σ-fashion, a second, *cis* bond not being observed.

The exchange constant was determined in the case of dimers, for all spatial configurations using the broken-symmetry Eqs. 2–4, the results being displayed in Fig. 2. It can be seen that the range of values for the angle θ the exchange constants calculated with Eqs. 2–4 verify consistently the relation $|J_R| < |J_Y| \leq |J_N|$, in agreement with other authors [54].

A second observation is that the differences between the coupling constants calculated based on the three methodologies synthesized by Eqs. 2–4 increase for smaller values of the angle θ. This result may be correlated with the orbital overlap, keeping in mind that the approach by Noodleman et al. [31, 32, 38] is valid in the orbital orthogonality (low overlap) limit, whereas the one by Ruiz et al. [39, 40] is applicable in the strong overlap limit. As it will be shown elsewhere in this section, at smaller angles θ, the $d_{z^2} - \pi*$ orbital overlap between the metal ion and the organic ligand is larger, suggesting that the approach by Ruiz et al. may be more applicable in that range than the one by Noodleman et al.

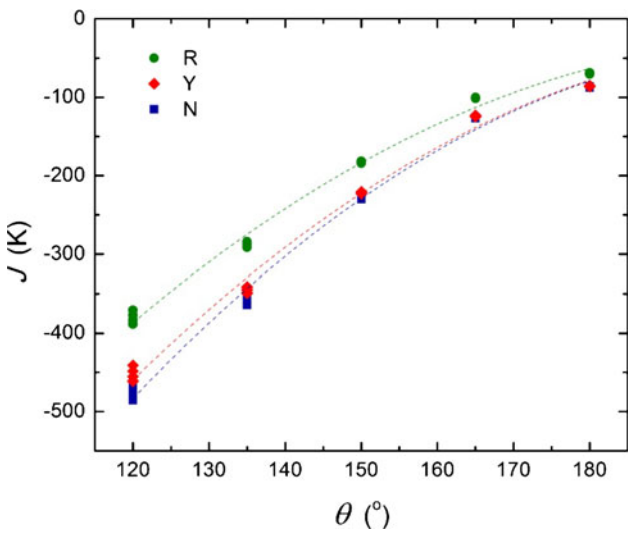

Fig. 2 Exchange coupling constants calculated by BS/DFT for the $\{(HCN)[Mn^{III}P]^+[TCNE]^-Li^+\}$ dimers as a function of θ, for all values of φ and constant $\psi = 90°$, at DFT/BP86/6-31G* level, using Eq. 2 (N), Eq. 3 (R), and 4 (Y)

The exchange maps were calculated for various spatial configurations for extended systems, based on Eq. 7, and for dimers, using Eq. 4. Because of the similar patterns observed, we display in Fig. 3 only the results obtained from the band calculations. The first observation is that the exchange constant is negative for all cases, indicating antiferromagnetic interactions between the $S_1 = 2$ spin on Mn(III) and the $S_2 = 1/2$ spin on $[TCNE]^{\cdot-}$, leading to ferrimagnetic behavior.

To further analyze the relationship between the exchange maps obtained for dimers and extended systems, we represent in Fig. 4 the values resulting from band calculations versus the values obtained for the dimers. The data lie almost on a straight line clearly indicating strong correlations between the two sets of calculations, and the consistency of our approach. The linear fits performed to the exchange constants calculated using Eqs. 2, 4, and 3 provided slopes of 0.83, 0.88, and 1.03, respectively.

To better understand these results, we should interpret the data of Fig. 2 by making reference to the structure shown in Fig. 1. At $\theta = 180°$, when the N≡C–group is aligned along the z axis (doted line in Fig. 1), the ψ angle does not change the overlap between the $\pi*$ orbital of $[TCNE]^{\cdot-}$ and the d orbitals of the Mn^{III} ion. It results that the ψ dependence of J cannot be significant in that range of θ, and the high plateau seen in Fig. 3 confirms this argument. When θ is decreased to 120°, the change of the angle ψ causes a significant variation of J, as the $[TCNE]^{\cdot-}$ anion is tilted toward the porphyrin plane, leading to different overlaps and varying the delocalization of the electron. For $\psi \sim 90°$, the tilt determines the largest possible $d_{z^2} - \pi*$ orbital overlap and, indeed, the exchange constant is largest in absolute value.

At $\psi = 0°$ (or 180°), changes in θ do not affect significantly the overlap between the d orbitals of the Mn^{III} ion and the $\pi*$ of $[TCNE]^{\cdot-}$. The d_{z^2} and $\pi*$ orbitals are orthogonal leading to weak ferromagnetic spin coupling, but the other interaction channels with $\pi*$, for instance through d_{xz} and d_{yz} orbitals make possible the spin delocalization and an overall small antiferromagnetic interaction, as seen in Fig. 3. When $\psi \sim 90°$, the variation of θ bends the TCNE plane toward the porphyrin, causing large differences in the $d - \pi*$ orbital overlap and wide changes in J.

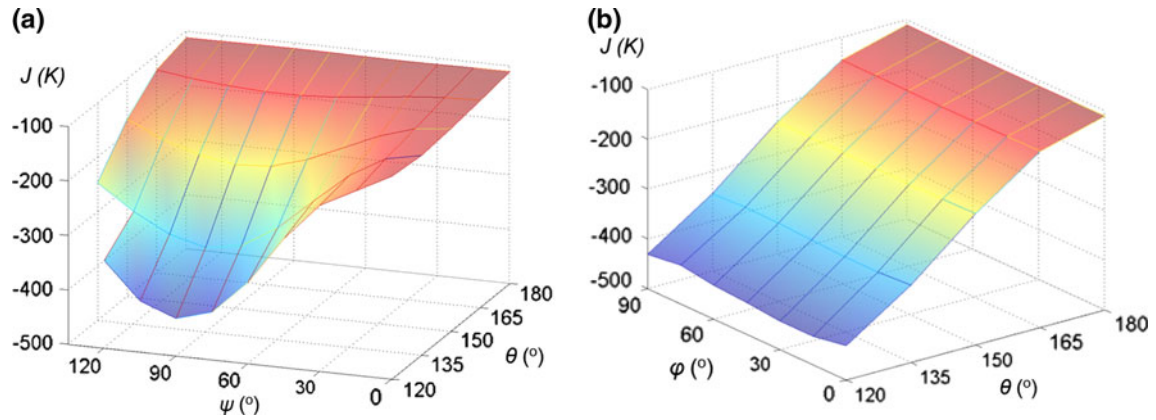

Fig. 3 Exchange coupling constants calculated by BS/DFT at BP86/6-31G* level, for $[Mn^{III}P]^{+}[TCNE]^{-}$ with PBC, using Eq. 7, at constant $\varphi = 0^{\circ}$ (**a**) and constant $\psi = 90^{\circ}$ (**b**). The values shown in this figure are also displayed in a table in the supplementary materials

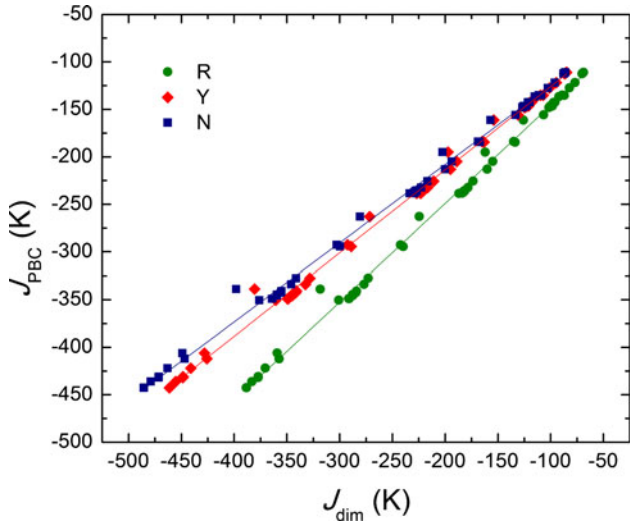

Fig. 4 Exchange coupling constants for $[Mn^{III}P]^{+}[TCNE]^{-}$ with PBC, using Eq. 7, versus the corresponding values obtained for the $\{(HCN)[Mn^{III}P]^{+}[TCNE]^{-}Li^{+}\}$ dimers, using Eq. 2 (N), Eq. 3 (R), and 4 (Y), at DFT/BP86/6-31G* level

A careful look at Fig. 3 shows that θ and ψ are correlated. They both have a similar slow variation at $\theta = 180°$ and $\psi = 0°$, and they both display a rapid increase in the strength of the exchange interaction at $\theta \sim 120°$ when varying ψ and at $\psi \sim 90°$ when varying θ. The correlation between θ and ψ dependence of J can be noticed when moving on the surface from $\theta = 180°$ and $\psi = 0°$ corner to the minimum at $\theta = 120°$ and $\psi = 90°$, as the variation in J is roughly similar. The reason behind this correlation is that the θ and ψ variations affect the overlap between the d orbitals of the Mn^{III} ion and the π^* of $[TCNE]^{\cdot -}$ in the same way. A given geometrical configuration (and the corresponding orbital overlap) can be reached by either fixing θ and changing ψ or the opposite.

The situation is very different in the case of φ. The rotation of the TCNE plane around the z axis (dotted line in Fig. 1) does not vary drastically the orbital overlap and cannot change significantly the exchange coupling constant. The shape of the surface indicates that the key variable is, in fact, angle θ.

Given the wide variation of the exchange constant with the orientation of the $[TCNE]^{\cdot -}$ anion with respect to the porphyrin plane, an interesting question to address is whether the configurations that lead to strongest J are positioned in a region where the energy of the ground state is lowest. To answer this question, we plot the energy surface for the LS state, calculated for the extended $[Mn^{III}P]^{+}[TCNE]^{-}$ systems with PBC as a function of the angles θ, φ, and ψ (see Fig. 5). The minimum value of the energy is obtained on the $\varphi = 0$ surface for $\theta = 150°$ and $\psi = 105°$, whereas on the $\psi = 90°$ surface for $\theta = 150°$ and $\varphi = 30°$. Comparing Figs. 3 and 5, we can conclude that there is a fair correspondence between the structures that cause a strong exchange and those that lead to a low energy of the LS state.

To further check the consistency of our results, we performed a DFT geometry optimization of the $[Mn^{III}P]^{+}[TCNE]^{-}$ extended system with PBC at BP86/6-31G* level. The optimized structure is characterized by the following key parameters: $r = 2.198$ Å, $\theta = 141.72°$, $\varphi = 21.14°$, $\psi = 99.42°$. All these structural parameters are in the correct range, where the energy of the low-spin state is minimal and the strength of the exchange constant maximal, especially when keeping in mind the interval of 15° for the angles determining the mesh.

The optimized geometry was further used for a comparison of the role of the DFT functional and of the basis set on the exchange constant. Table 1 displays the exchange constants obtained by BS/DFT using two gradient corrected functionals, BP86 and BLYP, and a hybrid functional B3LYP, with 6-31G*, 6-31+G*, as well as 6-311G* basis functions. It can be seen that the gradient corrected functionals lead to a systematic and significant overestimation of the exchange constant, the BP86 providing slightly better

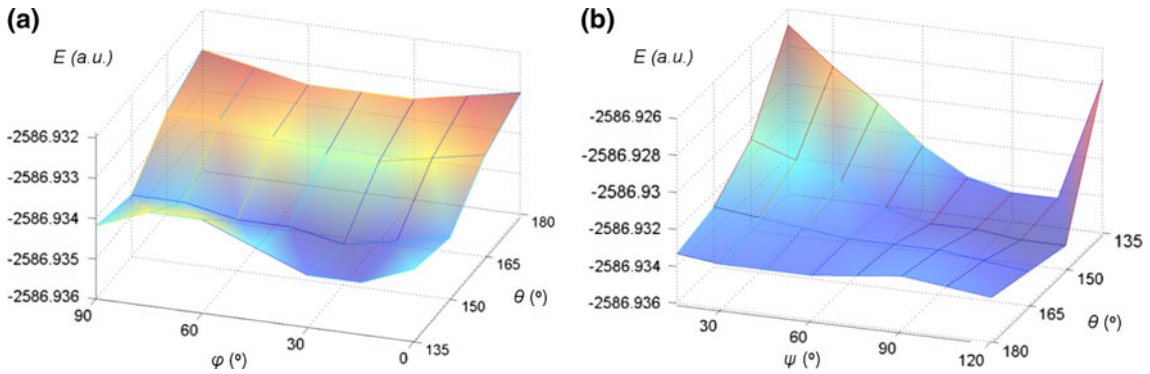

Fig. 5 Energy of the LS state calculated by BS/DFT at BP86/6-31G* level, for the $[Mn^{III}P]^{+}[TCNE]^{-}$ extended system with PBC, at constant $\psi = 90°$ (*left*) and constant $\varphi = 0°$ (*right*). The values shown in this figure are also displayed in a table in the supplementary materials

Table 1 Exchange coupling constants, expressed in K, for $[Mn^{III}P]^{+}[TCNE]^{-}$ with PBC and for the $\{(HCN)[Mn^{III}P]^{+}[TCNE]^{-}Li^{+}\}$ dimers, using the geometry optimized in band calculations for various DFT functionals and basis sets

DFT functional	Basis set					
	6-31G*		6-31+G*		6-311G*	
	Dimer	PBC	Dimer	PBC	Dimer	PBC
BP86	−406.5	−408.7	−418.6	−418.2	−405.4	−405.0
BLYP	−412.9	−414.3	−423.0	−420.8	−411.9	−409.9
B3LYP	−219.0	−212.4	−220.2	–[a]	−215.4	−207.7

[a] The calculation did not converge

results than the BLYP functional. As expected [27, 55], the introduction of the Hartree–Fock exchange in the hybrid functional B3LYP leads to much weaker exchange couplings, which are, as it will be shown in next section, in better agreement with experimental results.

The convergence problems and the very demanding computational costs of using B3LYP on extended systems, using PBCs, prompted us to make a compromise and use the BP86 functional for band calculations. However, when dealing with dimers, for which the computational costs are low, B3LYP is clearly the functional of choice.

Looking at the choice of the basis set, we note that the differences in the exchange constant are modest, less than 4%. A slight overestimation of the exchange coupling is observed, as expected, when using diffuse functions, due to the larger orbital overlap resulting in this case. In agreement with the previous results [27], once polarization effects are included, the differences between the basis sets do not lead to significant variations of the exchange constants.

4.2 Comparison of theoretical calculations with experimental results

In the previous section, we compared the exchange constants obtained for Mn-porphyrin extended systems and for the dimers and showed that the former are systematically lower by a factor of 0.862 than the later. It is important to compare the results of the calculations also with respect to the experimental data. One such set of experimental results was reported earlier [16, 17] for the manganese-porphyrin compounds [MnTPP][TCNE]·*x*S, (S = *ortho*-xylene, and *ortho*-dichlorobenzene). The fits of the dc susceptibility data to a model of alternating classical and quantum spins provided intrachain exchange constants of $J_{exp} = -83$ K and $J_{exp} = -140$ K, respectively [16, 17]. Other authors have reported values of the intrachain magnetic coupling in the range −350 to −30 K [25].

In order to compare our theoretical calculations with experimental results [7, 8, 24], we performed BS/DFT calculation for the $\{(HCN)[Mn^{III}P]^{+}[TCNE]^{-}Li^{+}\}$ dimmers, for the specific structures, selecting carefully the distance r between Mn–N_{TCNE}, and the angles θ, ψ, and φ. The results of the computations and the comparison with the experiments are summarized in Fig. 6, as a function of the most significant angle θ, Mn–$(N\equiv C)_{TCNE}$. We note that along with the plot of the theoretical exchange constant versus θ we also added a plot of the mean-field critical temperature Θ_{CW} versus θ.

Based on the Curie–Weiss law $\chi = C/(T - \Theta_{CW})$, the so-called Curie–Weiss temperature, Θ_{CW}, can be determined experimentally from the fit of the experimental data plotted as the inverse static magnetic susceptibility versus temperature to the Curie law. The extrapolated linear fit $\chi^{-1} = T/C - \Theta_{CW}/C$ intercepts the abscissa at $T = \Theta_{CW}$, which is positive for ferromagnets and negative for antiferromagnets. In the case of ferrimagnets, such as the [MnTPP][TCNE] systems studied here, care should be taken as the high T behavior leads to a negative mean-field temperature (the Néel temperature), and only a fit at intermediate T can provide a reasonable estimation of the mean-field Curie–Weiss temperature [24].

From Fig. 6, it can be seen that the range of values of the exchange interaction (represented in absolute value)

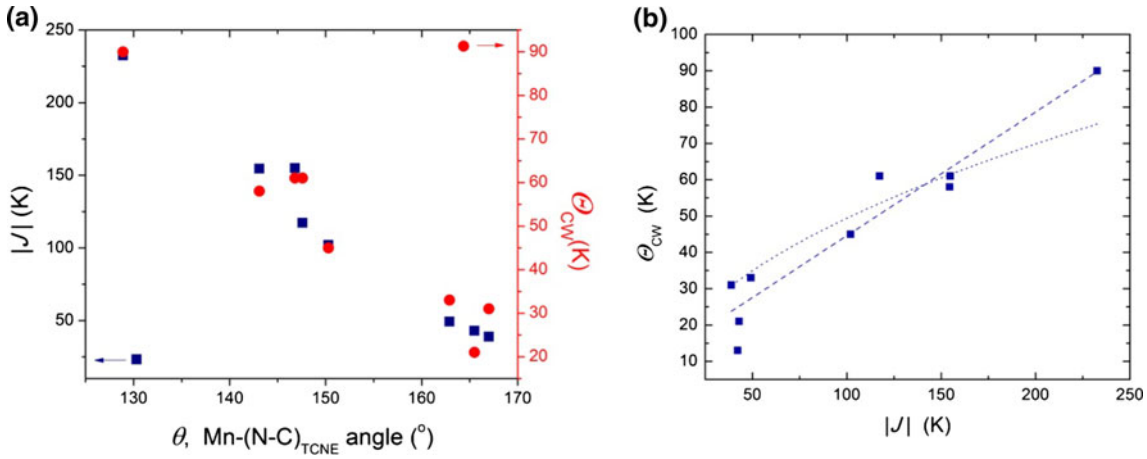

Fig. 6 **a** Experimental mean-field critical temperatures for [Mn-porphyrin][TCNE] compounds (from Ref. [25]) and calculated strength of exchange coupling for the {(HCN)[$Mn^{III}P$]$^+$[TCNE]$^-$$Li^+$} dimers (at BS-DFT/B3LYP/6-31G* level) versus the Mn–(N≡C)$_{TCNE}$ angle, θ. **b** Experimental mean-field critical temperature versus corresponding calculated exchange coupling from **a**)

calculated by BS/DFT for the dimers is between ~ -250 K and ~ -50 K, in relative agreement with the experimental values reported by several authors (-140 to -83 K [16, 17] and -350 to -30 K [25]). The values obtained by calculations of extended systems, with PBC, are smaller by about 0.862, as already seen in Fig. 4, and systematically larger than the experimental values.

Furthermore, analyzing the overall dependence of both $|J|$ and Θ_{CW} on the angle θ, we note that both the mean-field critical temperature and the strength (absolute value) of the magnetic coupling constant decrease with the Mn–(N≡C)$_{TCNE}$ angle. Plotting, for each such angle, Θ_{CW} versus $|J|$ we observe a clear correlation, although the mathematical nature of the relationship is hard to distinguish. For a molecular magnet with comparable interactions in all three-dimensions, a direct proportionality between the mean-field critical temperature and the strength of the magnetic interaction is expected ($\Theta_{CW} \sim J$), whereas for chain systems the critical temperature is expected to depend on the square root of the product between the intra- and interchain exchange constants ($\Theta_{CW} \sim T_c \sim \sqrt{J_{intra} J_{inter}}$) [3, 16, 17].

A comment of interest concerns the location of the experimental structures on the calculated energy surfaces plotted in Fig. 6. Although the experimental value for the angle θ varies over a wide range (125°–167°), most systems tend to concentrate in the range 140°–150°, where E_{LS} does have low values. Moreover, when the angle θ seems out of range, there is a tendency for the value of angle ψ to compensate and tilt the TCNE plane toward the porphyrin plane.

4.3 Density of states and electronic structure

The density of states (DOS) from unrestricted DFT calculations of the extended [$Mn^{III}P$]$^+$[TCNE]$^-$ system is represented in Fig. 7. In Fig. 7, we also display the diagram of the energy levels of the molecular orbitals determined by unrestricted DFT computations for the {(HCN)[$Mn^{III}P$]$^+$[TCNE]$^-$$Li^+$} dimer, as well as the electron density for the most relevant molecular orbitals.

To clarify the magnetic coupling mechanism in these systems, we parallel and contrast the two approaches pictured in Fig. 7, discussing the one-electron crystalline orbitals (CO) and the corresponding energy bands and the one-electron molecular orbitals (MO) and their energy levels. We note that the two calculations provide consistent results, although the two scales of energy are different, with lower values being obtained for the dimer, likely due to the presence of the terminating Li^+ ions and HCN group. However, if we keep in mind the range of energy for the orbitals of interest, we find, as we argue elsewhere, that the intervals are the same, about 4 eV for both the infinite chain and the isolated dimer.

The lowest band of interest is the spin-up one with high contribution from the $3d_{xy}$ Mn^{III} AO, located at -7.41 eV. It is followed at -7.34 eV by another α band with contributions from both $3d_{xz}$ and $3d_{yz}$ orbitals. As seen on the right side of Fig. 7, the corresponding spin-up MOs are located at -9.90 and -9.83 eV, respecting the same order and having almost identical electron densities.

At -7.20 eV, the superimposed α and β bands are localized on the porphyrin, with corresponding MOs on the dimer at ~ -9.40 eV. Similarly, the COs at -6.45 and -6.22 eV, showing overlap of spin-up and spin-down, are delocalized over the porphyrin with some d_{xz} and d_{yz} character. The corresponding MOs of the dimer are found at -8.68 and -8.61 eV.

In the same range are also found the spin-down and the spin-up states with π_{TCNE} character. More precisely, the β band starts at -6.65 eV, with a maximum in the $k = 0$

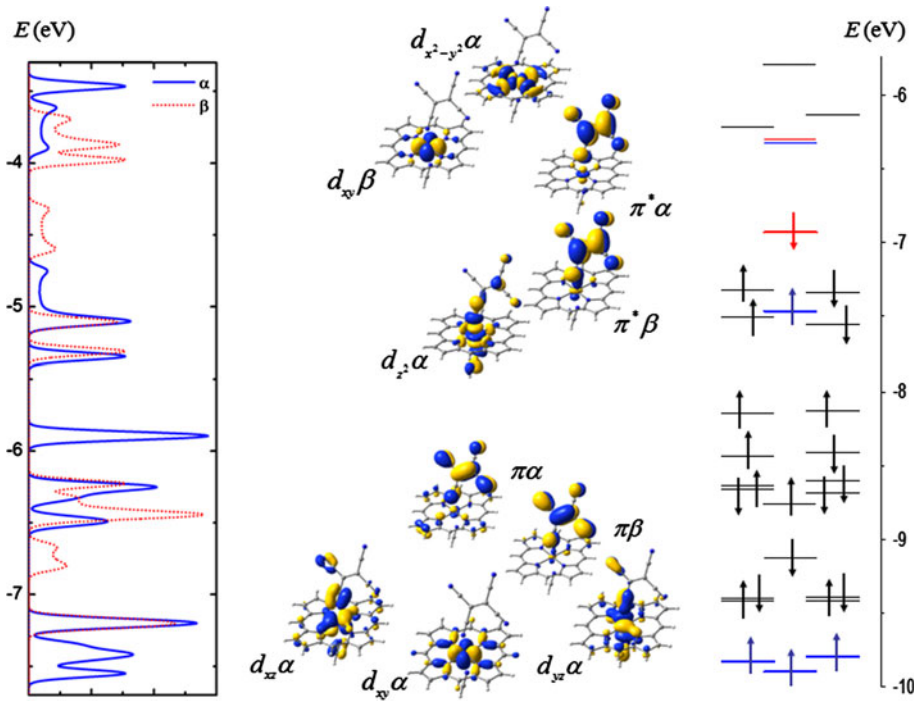

Fig. 7 Density of states calculated by unrestricted DFT at BP86/6-31+G* level for $[Mn^{III}P]^{+}[TCNE]^{-}$ in its ground-state ferrimagnetic configuration (*left*). Electronic structure calculated by unrestricted DFT at the same BP86/6-31+G* level for the $\{(HCN)[Mn^{III}P]^{+}[TCNE]^{-}Li^{+}\}$ dimer, at optimized geometry for the infinite system (*right*). Electron densities of MOs determined for the dimer (0.03 e/bohr^3) (*center*)

limit, whereas the α band lies at −6.45 eV, with a minimum in the same limit. In a similar way, the orbitals $\pi\beta$ and $\pi\alpha$ shown in Fig. 7 are located at −9.13 and −8.76 eV, respectively.

At −5.88 eV for the infinite chain and −8.14 eV in the case of the dimer, the α states are mixed, with a strong component from porphyrin π orbitals and some contribution from d_{xz} and d_{xy} orbitals. Moving further up in energy, the overlapping α and β bands situated at −5.35 and −5.10 eV, the COs having large contributions from the porphyrin π* orbitals mixed with some $3d_{xz}$ and $3d_{yz}$ orbitals of Mn. The corresponding MOs have energies of −7.55 and −7.35 eV, respectively.

The CO with strong Mn $3d_{z^2}$ contribution is spin-up, located at −5.13 eV, in the low wave number limit, and continuing up to −4.64 eV. The energy of the related MO is −7.46 eV. The electron density pictured in Fig. 7 indicates strong mixing of the $3d_{z^2}$ and π^*_{TCNE} orbitals, and percolation of the orbital along the chain. The delocalization of the electron of the Mn ion along the chain through the ligand allows the lowering of the kinetic energy and is consistent with the strong intrachain magnetic interaction.

The highest occupied band, starting at −4.68 eV and extending up to −4.21 eV, is spin-down and dominated by the π* of TCNE but with a contribution from the d_{Z^2} orbital. The corresponding MO is located at −6.96 eV and displays, just as the highest α orbital, strong delocalization along the chain.

A significant difference in the results of the computation for the extended system, with PBC, and for the dimer, regards the first excited orbital. In the band picture, the LUCO is spin-down, with mainly d_{xy} character, being located at −3.98 eV. Next to it, at −3.86 and −3.67 eV, lie the other two β spin COs, with contributions from the d_{yz} and d_{xz} orbitals, respectively. The first excited spin-up CO orbital lies higher in energy, extending from −3.95 eV to the low wave number limit of −3.55 eV and is dominated by the $\pi^*\alpha$ of TCNE. Unlike the periodic system, in the case of the dimer, the LUMO is spin-up, $\pi^*_{TCNE}\alpha$ and located at −6.33 eV, whereas at only 0.05 eV higher, the LUMO+1 is the $d_{xy}\beta$. The next two β MOs, d_{yz} and d_{xz}, are situated at −6.22 and −6.14 eV, respectively.

The highest orbital represented in Fig. 7 is the remaining of the five 3*d* AOs of the Mn^{III} ion, the empty spin-up orbital $d_{x^2-y^2}$, located at −3.46 eV in the band picture and −5.79 eV in the case of the dimer.

Ending this discussion, we note that of the four singly occupied α MOs originating from the Mn^{III} 3*d* AOs three orbitals are grouped together at an interval of about 2.4 eV below the d_{Z^2} orbital, interval that quantifies the splitting caused by the ligand field. Although for an elongated octahedral environment around the Mn^{III} ion, one would expect that the d_{xz} and d_{yz} orbitals would lie lowest our results reflect the reverse. The switch in energy is likely related to the σ character of the bond between the d_{xy} and the N atoms in the porphyrin, which provides larger overlap and lowers the energy significantly.

The delocalization seen in the Mn-porphyrin bridged by TCNE in both the HOMO-1 and HOMO indicates strong covalent character, with a large orbital overlap and a large

transfer integral. As a consequence, the total energy of the system is lowered, because the kinetic energy decreases for antiparallel spins, due to their ability to transfer over on to each other's site. Moreover, analyzing Fig. 7, we note that the lowest lying virtual excitation is from the $\pi^*\beta$ HOMO localized on TCNE to the $d_{xy}\beta$ LUMO+1 strongly localized on the Mn^{III} ion and its N neighbors on the porphyrin. Any other back and forth transfer of the spins involves significantly higher excitations energies, making any other virtual charge transfer unlikely. The configuration mixing of the ground-state $d_{xy}\alpha^1 d_{xz}\alpha^1 d_{yz}\alpha^1 d_{z^2}\alpha^1\pi^*\beta^1$ of [Mn-porphyrin]$^+$[TCNE]$^-$ and the excited, charge transferred state $d_{xy}\alpha^1 d_{xz}\alpha^1 d_{yz}\alpha^1 d_{Z^2}\alpha^1\pi^*\beta^0 d_{z^2}\beta^1$ of [Mn-porphyrin]^0[TCNE]^0 provides the main path for antiferromagnetic interaction. This mechanism of kinetic exchange is supported by the dependence of the intrachain exchange constant on the Mn-$(N\equiv C)_{TCNE}$ bond angle. The increase in the strength of the intrachain interaction when the angle decreases from 180° to about 140° can be explained based on the $d_{z^2} - \pi* \sigma$ bonding and orbital overlap increase, as suggested by other studies [24, 26].

5 Conclusion

We reported calculations providing the magnetic exchange for [Mn^{III}(porphyrin)]$^+$[TCNE]$^-$ systems. Broken-symmetry DFT calculations of model structures, extended [MnP]$^+$[TCNE]$^-$ systems and {(HCN)[Mn^{III}P]$^+$[TCNE]$^-$$Li^+$} dimers, obtained by varying systematically the main angles, allowed the construction of maps of the exchange coupling constant, which revealed the determinant role of the Mn-$(N\equiv C)_{TCNE}$ bond angle. The exchange coupling constants resulting from DFT calculations of extended systems, with periodic boundary conditions in the Ising approximation, were found to be generally consistent with those obtained for the dimers. The coupling constant calculated for dimers varies significantly with the type of broken-symmetry approach, as it is sensitive to the overlap between magnetic orbitals. We found that the approach of Noodleman et al. [31, 32, 38] is more suited in the orthogonal limit, the one of Ruiz et al. [39, 40] in the strong overlap limit, whereas the expression of Yamaguchi et al. [41, 42] leads to intermediate values, in agreement with other reports [54].

The strength of the exchange constant depends strongly on the DFT functional and weakly on the basis set used. Hybrid functionals, such as B3LYP, outperform gradient corrected functionals such as BP86 and BLYP. Using B3LYP with basis sets with polarization functions, we obtained for dimers values of the exchange constant in semi-quantitative agreement with the experimental values, as well as with the mean-field critical temperatures. When dealing with dimers, for which the computational costs are low, B3LYP is clearly the functional of choice. BP86 provides slightly better results than BLYP but both significantly overestimate the magnetic coupling. They may be used for periodic systems, for semi-qualitative analyses, when, due to convergence problems and demanding computational costs, B3LYP is not a practical option.

Finally, the electronic structure calculations for the extended systems and for the dimers provided a density of states and a discrete energy spectrum that allowed magneto-structural correlations, which emphasized the key role of the $d_{z^2} - \pi*$ orbital overlap. The analysis of the energy spectrum suggests that the mixing of the ground state and the first excited state, involving a charge transfer from the cyanocarbon ligand to the metal ion, is consistent with the kinetic exchange as main cause of intrachain ferrimagnetic ordering in [MnTPP][TCNE] systems.

Acknowledgments The authors acknowledge financial support from the Romanian Ministry of Education and Research through the CNCSIS-UEFISCSU research grant PN2-Idei-PCCE-239/2010, contract no. 9/2010.

References

1. Kahn O (1993) Molecular magnetism. VCH Publishers, New York
2. Miller JS, Drillon M (eds) (2002) Magnetism: molecules to materials. Wiley-VCH, Weinheim
3. Gîrţu MA, Fahlman M (2009) In: Nalwa HS (ed) Magnetic nanostructures, hybrid organic-inorganic nanostructured magnets. American Scientific Publishers, Stevenson Ranch, pp 359–433
4. Miller JS, Calabrese JC, McLean RS, Epstein AJ (1992) Adv Mater 4:498
5. Sugiura K-I, Arif A, Rittenberg DK, Schweizer J, Ohrstrom L, Epstein AJ, Miller JS (1997) Chem Eur J 3:138
6. Brandon EJ, Sugiura K-I, Arif AM, Liable-Sands A, Rheingold AL, Miller JS (1997) Mol Cryst Liq Cryst 305:269
7. Sugiura K-I, Mikami S, Tanaka T, Sawada M, Manson JL, Miller JS, Sakata Y (1997) Chem Lett 1071
8. Brandon EJ, Arif AM, Miller JS, Sugiura K-I, Burkhart BM (1998) Crystal Eng 1:97
9. Brandon EJ, Burkhart BM, Rogers RD, Miller JS (1998) Chem Eur J 4:1938
10. Brandon EJ, Arif AM, Burkhart BM, Miller JS (1998) Inorg Chem 37:2792
11. Brandon EJ, Rittenberg DK, Arif AM, Miller JS (1998) Inorg Chem 37:3376
12. Rittenberg DK, Sugiura K-i, Sakata Y, Guzei IA, Rheingold AL, Miller JS (1999) Chem Eur J 5:1874
13. Rittenberg DK, Sugiura K-I, Sakata Y, Mikami S, Epstein AJ, Miller JS (2000) Adv Mater 12:126
14. Hibbs W, Rittenberg DK, Sugiura K-I, Burkhart BM, Morin BG, Arif AM, Liable-Sands L, Rheingold AL, Sundaralingam M, Epstein AJ, Miller JS (2001) Inorg Chem 40:1915
15. Epstein AJ, Wynn CM, Gîrţu MA, Brinckerhoff WB, Sugiura K-i, Miller JS (1997) Molec Cryst Liq Cryst 305:321
16. Wynn CM, Gîrţu MA, Brinckerhoff WB, Sugiura K-I, Miller JS, Epstein AJ (1997) Chem Mater 9:2156
17. Wynn CM, Gîrţu MA, Sugiura K-i, Brandon EJ, Manson JL, Miller JS, Epstein AJ (1997) Synth Met 85:1695

18. Wynn CM, Gîrţu MA, Miller JS, Epstein AJ (1997) Phys Rev B 56:315
19. Wynn CM, Gîrţu MA, Miller JS, Epstein AJ (1997) Phys Rev B 56:14050
20. Gîrţu MA, Wynn CM, Sugiura K-I, Miller JS, Epstein AJ (1997) J Appl Phys 81:4410
21. Gîrţu MA, Wynn CM, Sugiura K-I, Miller JS, Epstein AJ (1997) Synth Metals 85:1703
22. Lescouezec R, Toma LM, Vaissermann J, Verdaguer M, Delgado FS, Ruiz-Perez C, Lloret F, Julve M (2005) Coord Chem Rev 249:2691
23. Seiden J (1983) J Phys (Paris) Lett 44:L-947
24. Brandon EJ, Kollmar C, Miller JS (1998) J Am Chem Soc 120:1822
25. Ribas-Arino J, Novoa JJ, Miller JS (2006) J Mater Chem 16:2600
26. Koizumi K, Shoji M, Kitagawa Y, Taniguchi T, Kawakami T, Okumura M, Yamaguchi K (2005) Polyhedron 24:2720
27. Cimpoesu F, Ferbinteanu M, Frecuş B, Gîrţu MA (2009) Polyhedron 28:2039
28. Hohenberg P, Kohn W (1964) Phys Rev 136:B864
29. Kohn W, Sham LJ (1965) Phys Rev A 140:1133
30. Parr RG, Yang W (1989) Density-functional theory of atoms and molecules. Oxford University Press, New York
31. Noodleman L, Norman JG (1979) J. Chem Phys 70:4903
32. Noodleman L (1981) J Chem Phys 74:5737
33. Bencini A, Totti F (2005) Int J Quant Chem 101:819
34. Daul CA, Ciofini I, Bencini A (2002) In: Sen KD (ed) Reviews of modern quantum chemistry, part II. World Scientific, Singapore, p 1247
35. Noodleman L, Peng CY, Case DA, Mouesca JM (1995) Coord Chem Rev 144:199
36. Nagao H, Nishino M, Shigeta Y, Soda T, Kitagawa Y, Onishi T, Yoshioka Y, Yamaguchi K (2000) Coord Chem Rev 198:265
37. Ruiz E (2004) Struct Bonding 113:71
38. Noodleman L, Davidson ER (1986) Chem Phys 109:131
39. Ruiz E, Alemany P, Alvarez S, Cano J (1997) J Am Chem Soc 119:1297
40. Ruiz E, Cano J, Alvarez S, Alemany P (1999) J Comput Chem 20:1391
41. Mitani M, Mori TakanoY, Yamaki D, Yoshioka Y, Yamaguchi K (2000) Chem Phys 113:4035
42. Onishi T, Takano Y, Kitagawa Y, Kawakami T, Yoshioka Y, Yamaguchi K (2001) Polyhedron 20:1177
43. Dai D, Whangbo M-H (2003) J Chem Phys 118:29
44. Shoji M, Koizumi K, Kitagawa Y, Kawakami T, Yamanaka S, Okumura M, Yamaguchi K (2006)). Chem Phys Lett 432:343
45. Gorelik EV, Ovcharenko VI, Baumgarten M (2008) Eur J Inorg Chem 2837
46. Nakanashi Y, Kitagawa Y, Saito T, Kataoka Y, Matsui T, Kawakami K, Okumura M, Yamaguchi K (2009) Int J Quantum Chem 109:3632
47. Frisch MJ, Trucks GW, Schlegel HB, Scuseria GE, Robb MA, Cheeseman JR, Montgomery JJA, Vreven T, Kudin KN, Burant JC, Millam JM, Iyengar SS, Tomasi J, Barone V, Mennucci B, Cossi M, Scalmani G, Rega N, Petersson GA, Nakatsuji H, Hada M, Ehara M, Toyota K, Fukuda R, Hasegawa J, Ishida M, Nakajima T, Honda Y, Kitao O, Nakai H, Klene M, Li X, Knox JE, Hratchian HP, Cross JB, Bakken V, Adamo C, Jaramillo J, Gomperts R, Stratmann RE, Yazyev O, Austin AJ, Cammi R, Pomelli C, Ochterski JW, Ayala PY, Morokuma K, Voth GA, Salvador P, Dannenberg JJ, Zakrzewski VG, Dapprich S, Daniels AD, Strain MC, Farkas O, Malick DK, Rabuck AD, Raghavachari K, Foresman JB, Ortiz JV, Cui Q, Baboul AG, Clifford S, Cioslowski J, Stefanov BB, Liu G, Liashenko A, Piskorz P, Komaromi I, Martin RL, Fox DJ, Keith T, Al-Laham MA, Peng CY, Nanayakkara A, Challacombe M, Gill PMW, Johnson B, Chen W, Wong MW, Gonzalez C, Pople JA (2004) Gaussian 03, revision C.02. Gaussian, Inc., Wallingford
48. Becke AD (1998) Phys Rev A 38:3098
49. Perdew JP (1986) Phys Rev B 33:8822
50. Rassolov VA, Ratner MA, Pople JA, Redfern PC, Curtiss LA (2001) J Comp Chem 22:976
51. Becke AD (1988) Phys Rev A 38:3098
52. Lee C, Yang W, Parr RG (1988) Phys Rev B 37:785
53. Becke AD (1993) J Chem Phys 98:5648
54. Bencini A, Totti F (2009) J Chem Theory Comput 5:144
55. Cabrero J, Calzado CJ, Maynau D, Caballol R, Malrieu JP (2002) J Phys Chem A 106:8146